Poly(Acrylic Acid) Modification of Nd^{3+}-Sensitized Upconversion Nanophosphors for Highly Efficient UCL Imaging and pH-Responsive Drug Delivery

Bei Liu, Yinyin Chen, Chunxia Li, Fei He, Zhiyao Hou, Shanshan Huang, Haomiao Zhu, Xueyuan Chen, and Jun Lin**

In this work, a simple method is demonstrated for the synthesis of multifunctional core–shell nanoparticles $NaYF_4$:Yb,Er@$NaYF_4$:Yb@$NaNdF_4$:Yb@$NaYF_4$:Yb@PAA (labeled as Er@Y@Nd@Y@PAA or UCNP@PAA), which contain a highly effective 808-nm-to-visible UCNP core and a thin shell of poly(acrylic acid) (PAA) to achieve upconversion bioimaging and pH-sensitive anticancer chemotherapy simultaneously. The core–shell Nd^{3+}-sensitized UCNPs are optimized by varying the shell number, core size, and host lattices. The final optimized Er@Y@Nd@Y nanoparticle composition shows a significantly improved upconversion luminescence intensity, that is, 12.8 times higher than Er@Y@Nd nanoparticles. After coating the nanocomposites with a thin layer of PAA, the resulting UCNP@PAA nanocomposite perform well as a pH-responsive nanocarrier and show clear advantages over UCNP@$mSiO_2$, which are evidenced by in vitro/in vivo experiments. Histological analysis also reveals that no pathological changes or inflammatory responses occur in the heart, lungs, kidneys, liver, and spleen. In summary, this study presents a major step forward towards a new therapeutic and diagnostic treatment of tumors by using 808-nm excited UCNPs to replace the traditional 980-nm excitation.

1. Introduction

Ln^{3+} (lanthanide ion)-based upconversion nanoparticles (UCNPs) have attracted much attention as an emerging research field because of their remarkable properties, such as high chemical stability, low auto-fluorescence, high signal-to-noise ratio, excellent detection sensitivity, high penetration depth, and good biocompatibility, which make them promising candidates for application in many areas including healthcare, energy, detection, and security.[1–4] However, conventional UCNPs still face many challenges that limit their practical applications, such as low upconversion efficiency, undesired interactions between the lanthanide ions, monotonicity of the excitation wavelength, limited excitation light harvesting ability, as well as limited functionalities for imaging and therapy. To address these challenges, a hierarchical design of the core–shell UCNPs is required because it will not only suppress quenching mechanisms to allow efficient upconversion emission for bioimaging applications, but will also enable us to purposely introduce some electronic energy states to provide opportunities for manipulating the electronic excitation, energy transfer, and upconversion emission.[5–9] For example, recently core–shell cascade-sensitized Nd^{3+}/Yb^{3+}/Er^{3+} (Tm^{3+}) tri-doped UCNPs have been designed to shift the 980-nm excitation wavelength to a more biocompatible wavelength of 808 nm, resulting in superior penetrability and lower heating effect than in 980-nm sensitized UCNPs, because the water absorption at 808 nm is less than 1/20 of that at 980 nm.[10–13] However, despite the large absorption cross-section of Nd^{3+} and the high energy transfer effciency from Nd^{3+} to Yb^{3+} (up to 70%), the absolute quantum yields (QYs) of upconversion photoluminescence for the reported Nd^{3+}-sensitized core–shell nanoparticles remain either unevaluated or low due to the deleterious energy transfer between activators and Nd^{3+}.[14,15] Therefore, the high 808-nm NIR excited upconversion luminescence QYs were urgently desired for the use of low excitation intensities during in vitro/in vivo fluorescent imaging, thus reducing possible radiation-induced collateral effects to a minimum.

Besides upconversion luminescence imaging for diagnosis,[16,17] therapeutic applications of UCNPs have also been studied extensively. To achieve this, numerous surface modification methods of UCNPs have been proposed.[18–20] Among them, applying a mesoporous silica shell coating on the UCNPs is one of the most commonly used strategies.[21–23] However, the relatively low drug loading capacity and rapid drug release

Dr. B. Liu, Dr. Y. Chen, Dr. C. Li, Dr. F. He, Dr. Z. Hou, Dr. S. Huang, Prof. J. Lin
State Key Laboratory of Rare Earth Resource Utilization
Changchun Institute of Applied Chemistry
Chinese Academy of Sciences
Changchun 130022, China
E-mail: cxli@ciac.ac.cn; jlin@ciac.ac.cn
Dr. B. Liu, Dr. Y. Chen, Dr. F. He
University of the Chinese Academy of Sciences
Beijing 100049, China
Dr. H. Zhu, Prof. X. Chen
Key Laboratory of Optoelectronic Materials Chemistry and Physics
Fujian Institute of Research on the Structure of Matter
Chinese Academy of Sciences
Fuzhou 350002, China

DOI: 10.1002/adfm.201501582

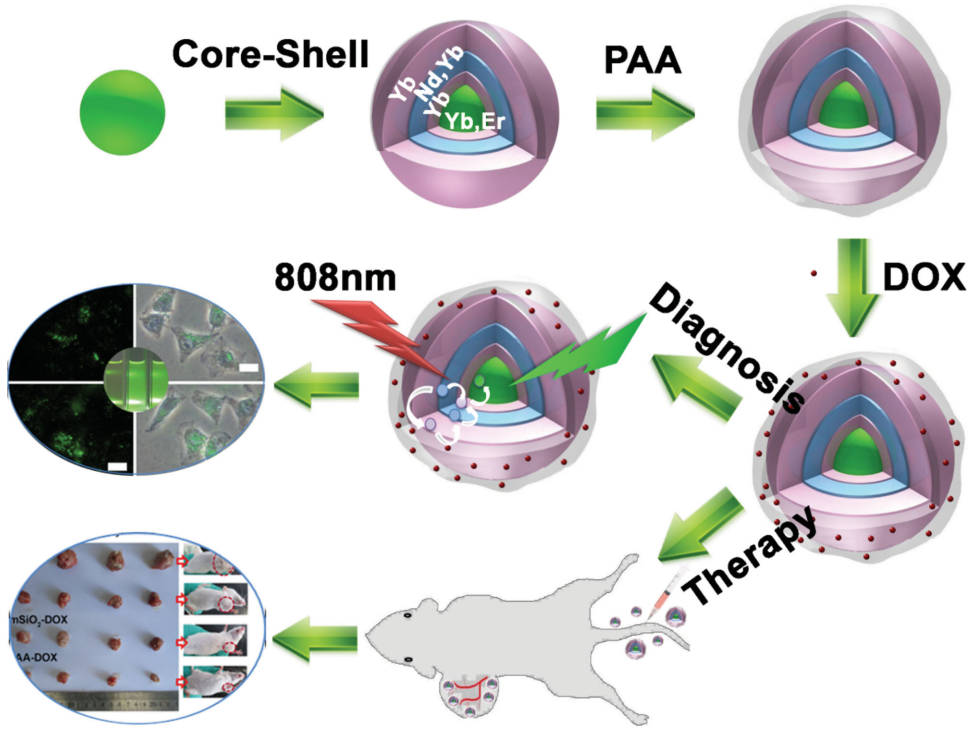

Scheme 1. Schematic illustration of the synthesis of core–shell structured $NaYF_4$:Yb, Er@$NaYF_4$:Yb@$NaNdF_4$:Yb@$NaYF_4$:Yb@PAA (labeled as UCNP@PAA) multifunctional nanoparticles and subsequent bio-applications in UCL imaging and anti-cancer therapy.

speed limit their bio-applications, resulting in poor therapeutic efficacy and relatively high cytotoxicity to normal cells. In order to tackle this issue, stimuli-responsive drug-delivery systems, especially pH-responsive drug vehicles that can take advantage of the extracellular acidic microenvironment of tumor tissues, have been widely explored.[24,25] Among them, the modification of UCNPs with PAA polymers has recently attracted a lot of attention because of its high drug loading storage capacity and sustained drug release profiles.[26–28] However, many of the reported PAA-coated UCNPs have some inevitable drawbacks, such as irregular morphology, multistep and complicated synthetic procedures, thick PAA shells or large particle size. For example, Kang et al. have reported PAA-modified $GdVO_4$ hollow spheres, but by a multistep and complicated method of a "ship-in-a-bottle" synthesis.[29] Wang and co-workers also designed novel pH-responsive eccentric-(concentric-UCNP@SiO_2)@PAA[30] and eccentric UCNP@PAA@SiO_2 nanocarriers,[31] but with an intermediate layer of SiO_2 to load anticancer drugs. Additionally, in vitro/in vivo anti-tumor therapy of these PAA-based nanoparticles has been rarely reported.

Herein, we report a facile and general method for the controlled synthesis of PAA-coated 808-nm excited UCNPs nanostructures, which is a major step forward towards anti-tumor chemotherapy utilizing 808-nm excited UCNPs to effectively access tumors without overheating effects. The optimal Er@Y@Nd@Y nanoparticles with a high absolute upconversion quantum yield of 0.18% in green emission (31 W cm^{-2}) have a significant 12.8× improvement of the UCL intensity than Er@Y@Nd nanoparticles under 808-nm excitation for biological imaging applications. When coated with a thin layer of PAA, the resulting UCNP@PAA nanocomposites are highly suited for use as anticancer drug delivery nanocarrier. Compared with UCNP@mSiO_2 nanoparticles, UCNP@PAA nanoparticles have obvious advantages, such as a smaller particle size, much higher drug delivery capacity, sustained drug release trends, and more effective anticancer chemotherapy activity, which were evidenced by in vitro/in vivo experiments.

2. Results and Discussion

2.1. Fabrication and Characterization of 808-nm-to-Visible Upconversion Nanoparticles $NaYF_4$:Yb,Er@$NaYF_4$:Yb@$NaNdF_4$:Yb@$NaYF_4$:Yb (UCNPs)

Recently, 808-nm-to-visible core–shell upconversion nanoparticles have sparked a rapidly growing interest because they hold great promise for solving long-standing problems associated with the conventional 980-nm-to-visible upconversion nanoparticles, such as lower penetrability and overheating effects.[11,15,32–36] Some researchers even believe that 808-nm excited UCNPs hold potential to become the next-generation luminophores.[13] In the present work, we describe a novel type of $NaYF_4$:Yb,Er@$NaYF_4$:Yb@$NaNdF_4$:Yb@$NaYF_4$:Yb (Er@Y@Nd@Y or UCNPs) multi-shell nanocrystals as an efficient 808-nm NIR-to-green luminescence emission probe for bioapplications. In detail, as shown in **Scheme 1** and **Figure 1**a, the Er@Y@Nd@Y nanoparticles were composed of a $NaYF_4$:20%Yb,2%Er core (the upconversion luminescence core), a $NaYF_4$:10%Yb shell (Shell 1; the energy transfer

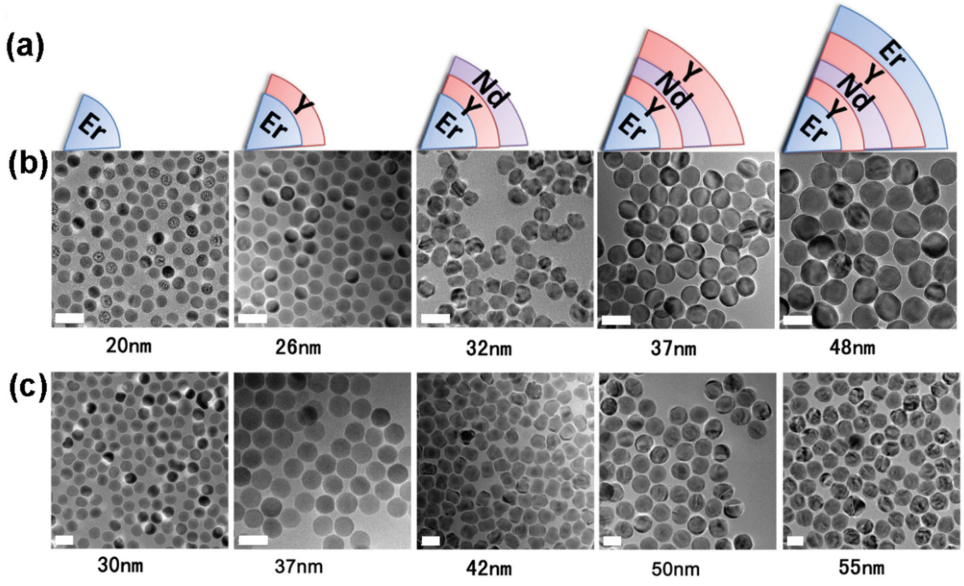

Figure 1. a) Schematic illustration of the core–shell structures of the various upconversion nanoparticles. b,c) TEM images of $NaYF_4$:Yb, Er (labeled as Er), $NaYF_4$:Yb, Er@$NaYF_4$:Yb (labeled as Er@Y), $NaYF_4$:Yb, Er@$NaYF_4$:Yb@$NaNdF_4$:Yb (labeled as Er@Y@Nd), $NaYF_4$:Yb, Er@$NaYF_4$:Yb@$NaNdF_4$:Yb@$NaYF_4$:Yb (labeled as Er@Y@Nd@Y), $NaYF_4$:Yb, Er@$NaYF_4$:Yb@$NaNdF_4$:Yb@$NaYF_4$:Yb@$NaYF_4$:Yb, Er (labeled as Er@Y@Nd@Y@Er) based on different core sizes of 20 nm (b) and 30 nm (c). All scale bars are 50 nm.

layer), $NaNdF_4$:10%Yb (Shell 2; the energy absorption layer) and another $NaYF_4$:10%Yb shell (Shell 3; the energy transfer layer and the luminescence quenching reduction layer). The corresponding high-angle annular dark field scanning TEM (HAADF-STEM) images, shown in Figure S1a,b of the Supporting Information, confirm the successful construction and core–shell structures of the Er@Y@Nd@Y nanoparticles. Furthermore, the elemental mapping images shown in Figure S1c–f of the Supporting Information confirm the multicomposite nanostructure of the UCNPs with uniformly distributed Nd, Y, F, and Yb elements. This successful fabrication of Er@Y@Nd@Y was achieved by successive hot injection of the shell precursors into the high-temperature reaction system without any intermediate steps, such as precipitation and washing, which was much more convenient than previously reported methods.[15] It is worth pointing out that the monodisperse $NaYF_4$:Yb,Er nanoparticles with different sizes (20 and 30 nm) can be synthesized successfully, and both of them could act as the core for the subsequent epitaxial shell deposition, as shown in Figure 1b,c.

Figure 1b,c also show that the nanoparticles of Er, Er@Y, and Er@Y@Nd@Y all have well-dispersed spherical morphologies, whereas the three-layer Er@Y@Nd nanoparticles show a highly anisotropic structure. In order to understand this phenomenon, we first ruled out the influence of the fabrication method, because the three-layer Er@Y@Nd nanoparticles that were synthesized stepwise have the same morphology as nanoparticles fabricated continuously by hot injection (Figure S2a–d of the Supporting Information). Then, $NaYF_4$:Yb,Er@$NaGdF_4$:Yb@$NaNdF_4$:Yb (Er@Gd@Nd) nanoparticles were successfully synthesized by the same continuous hot injection method. As shown in Figure S2e,f of the Supporting Information, the Er@Gd@Nd nanoparticles have a spherical morphology with a smooth surface, totally different from the morphology of Er@Y@Nd. Taking into account this difference, the core–shell morphology of Er@Y@Nd nanoparticles could be explained as follows: in the Er@Y@Nd nanoparticles, the ionic radius of Nd^{3+} (in the Shell 2; 0.098 nm) is much larger than Y^{3+} (in the Shell 1; 0.089 nm), thus the lattice of Shell 2 is compressed during the core–shell epitaxial growth process, resulting in the highly anisotropic structure of Er@Y@Nd. In contrast, the ionic radius of Nd^{3+} (in the Shell 2; 0.098 nm) in Er@Gd@Nd nanoparticlesis similar to that of Gd^{3+} (in the Shell 1; 0.094 nm), resulting in a uniform spherical core–shell morphology.[37]

Under 808-nm NIR laser excitation, as shown in **Figure 2**c and the insets, an obvious increase of the green emission intensity could be seen in Er@Y@Nd@Y in comparison to the Er@Y@Nd or Er@Y nanoparticles, which is likely due to the efficient suppression of surface-related deactivation and valid promotion of the interaction between the lanthanide dopants in Shell 3 with that in the Core/Shell 1/Shell 2 configuration. This change in the UC emission spectra was in agreement with the corresponding absolute quantum yield measurement at 540 nm (31 W cm^{-2}, under excitation at 808 nm) in Figure 2d, which shows that the Er@Y@Nd@Y nanoparticles have a relatively high absolute quantum yield of 0.18%, which is about 12.8 times higher than that of Er@Y@Nd nanoparticles. This large enhancement of the UC after simply coating the outermost shell may inspire a new way of thinking for the construction of more effective 808-nm excited UCNPs, which could promote efficient upconversion emission for bioimaging applications. It is worth noting that although the Er@Y@Nd nanoparticles synthesized here have the same core–shell architecture and doping concentrations (Yb, Nd, and Er) as those in Ref. 32, the quantum yield of Er@Y@Nd in our current test system is only 0.0134% (31 W cm^{-2}), much lower than that in Ref. 32 (0.11%

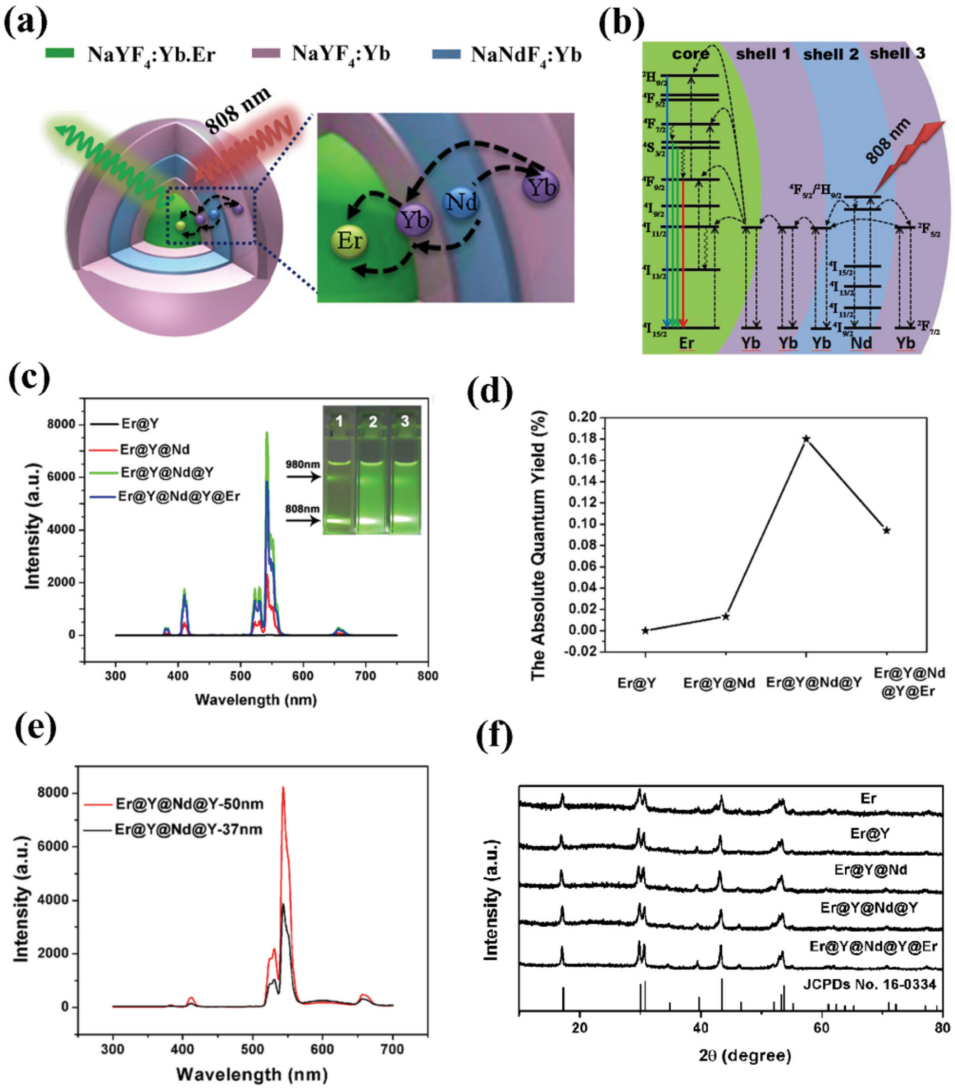

Figure 2. a) Schematic illustration of the mechanism of the upconversion processes excited at 808 nm in a multilayer Er@Y@Nd@Y nanoparticle system and b) the corresponding energy-level diagram. c) Upconversion emission spectra for various upconversion samples dispersed in cyclohexane (0.05 M) under 808-nm NIR laser excitation. The insets in panel (c) are photos of upconversion samples in cyclohexane solution exposed to a 980 nm laser (top) and 808 nm laser (bottom) (1: Er@Y@Nd, 2: Er@Y@Nd@Y, 3: Er@Y@Nd@Y@Er). d) The absolute quantum yield of various upconversion samples (measurement at 540 nm under excitation at 808 nm (31 W cm^{-2})). e) Upconversion emission spectra of Er@Y@Nd@Y based on different size of cores (0.05 M). f) XRD patterns of the as-prepared Er, Er@Y, Er@Y@Nd, Er@Y@Nd@Y, Er@Y@Nd@Y@Er, and the corresponding standard data of β-$NaYF_4$ (JCPDS No. 16–0334).

with a density of 20 W cm^{-2}). This is mainly because the testing equipment of the quantum yield varies from one to another. In fact, the accurate detection of the quantum yield remains a problem under the existing research conditions.

In recent years, green-emitting UCNPs were widely investigated because of their unique properties such as easy preparation, good luminescence stability as well as high color purity. The mechanism of the green emission excitation process at 808 nm in this multilayer nanoparticle system is shown in detail in the schematic illustration in Figure 2a and the corresponding energy-level diagram in Figure 2b. The overall energy transfer process can be described as follows: the Nd^{3+} ions in Shell 2 serve as the sensitizer to harvest 808-nm photons, resulting in a population of the $^4F_{5/2}$ state of Nd^{3+}. This photon energy from the sensitizer Nd^{3+} can be absorbed by Yb^{3+} ions in Shell 1 and Shell 3 through interionic cross-relaxation $[(^4F_{3/2})_{Nd}, (^2F_{7/2})_{Yb}] \rightarrow [(^4I_{9/2})_{Nd}, (^2F_{5/2})_{Yb}]$, followed by excitation-energy migration over the Yb^{3+} sublattice and finally entrapment by the activator ions of Er^{3+} embedded in the inner core. During this process, Shell 1, as a transition layer, serves as a shield to prevent quenching interactions between the activator and sensitizer, while Shell 3, as the energy transfer layer and the luminescence quenching reduction layer, can successfully enhance the UC luminescence. In other words, an efficient excitation energy transfer occurs from the sensitizer Nd^{3+} to the activator Er^{3+} in the Er@Y@Nd@Y nanoparticles through the Yb^{3+}-mediated Core/Shell 1/Shell 2/Shell 3 interface.

Further growth of the epitaxial shell on Er@Y@Nd@Y nanoparticles can also be achieved based on the same epitaxial seeded growth method. As shown in Figure 1b,c, the $NaYF_4$:Yb,Er shell layer (Shell 4) was successfully fabricated on the surface of Er@Y@Nd@Y, resulting in the formation of Er@Y@Nd@Y@Er with an increased nanoparticle size. However, as shown in Figure 2c and insets, further epitaxial growth of Shell 4 on the surface of the Er@Y@Nd@Y nanoparticles caused a decrease of the overall luminescence intensity under 808-nm laser excitation. This change in the trend was consistent with the results of the corresponding absolute quantum yield measurements (Figure 2d), which show that Er@Y@Nd@Y@Er nanoparticles show an absolute quantum yield of 0.094%, lower than that of Er@Y@Nd@Y nanoparticles. This phenomenon can perhaps be explained by over-broadening of the outside layers, which could affect the process of energy migration via the Yb^{3+} ions.[32]

Furthermore, the upconversion luminescence intensities of Er@Y@Nd@Y nanoparticles based on different core sizes were also investigated in detail. Figure 2e shows that Er@Y@Nd@Y nanoparticles based on 30-nm sized $NaYF_4$:Yb,Er had increased upconversion emission intensity compared with those based on 20-nm $NaYF_4$:Yb,Er, which was mainly because of the suppressed surface quenching. Since $NaGdF_4$ is also a commonly used substrate[38,39] for upconversion luminescence, we used $NaGdF_4$:Yb instead of $NaYF_4$:Yb to fabricate another kind of 808-nm excited core–shell nanoparticles: $NaYF_4$:Yb, Er@$NaGdF_4$:Yb@$NaNdF_4$:Yb@$NaGdF_4$:Yb (labeled as Er@Gd@Nd@Gd). As shown in Figure S3a of the Supporting Information, Er@Gd@Nd@Gd was successfully synthesized with the same epitaxial seeded growth method. However, the intensity of the upconversion luminescence decreased compared with that of Er@Y@Nd@Y at the same molar concentration, as shown in Figure S3b of the Supporting Information, suggesting that the $NaYF_4$ substrate performed better than $NaGdF_4$ in our current systems. The composition and phase purity of the UCNPs were also examined by XRD. Figure 2f shows that the diffraction peaks of Er, Er@Y, Er@Y@Nd, Er@Y@Nd@Y as well as Er@Y@Nd@Y@Er nanoparticles are all indexed exactly as a pure hexagonal phase structure β-$NaYF_4$ (JCPDS 16–0334). In conclusion, Er@Y@Nd@Y based on 30-nm sized $NaYF_4$:Yb,Er showed the highest upconversion intensity for all the particles investigated in this study and these findings confirmed our expectations that such novel nanoparticle systems are promising candidates for upconversion bio-applications.

2.2. Characterization of the UCNP@PAA Nanoparticles

As described above, we have successfully synthesized Er@Y@Nd@Y upconversion nanoparticles (labeled as UCNPs) with high upconversion luminescence intensity under 808-nm excitation. Besides upconversion luminescence imaging for diagnosis, therapeutic applications of UCNPs have also been studied extensively. Here, we demonstrate a simple synthetic route to produce a multifunctional UCNP-based pH-responsive drug delivery system, which involves a highly effective 808-nm-to-visible UCNP core and a thin shell of PAA (labeled as UCNP@PAA). The overall fabrication procedure and applications in simultaneous upconversion luminescence cell imaging and pH-responsive drug delivery of UCNP@PAA are shown in Scheme 1. In short, the synthesis process consists of two main steps: i) the conversion of the OA-capped UCNPs to cetyltrimethylammonium bromide (CTAB) modified UCNPs; ii) the as-synthesized UCNP–CTAB nanoparticles were further coated with concentric PAA shells upon addition of PAA solution and isopropyl alcohol. The experiments showed that the PAA molecules self-assembled around UCNP–CTAB to yield UCNP@PAA core–shell nanoparticles, which is probably due to the change in interfacial energy between PAA, the UCNPs, and the solvent, likely resulting in a minimum interfacial energy.[30,31] Compared with several other PAA coating methods,[29,40] our PAA coating method can be carried out at room temperature simply by magnetic stirring or ultrasonic treatment. This facile, general, and highly reproducible synthetic route for UCNP@PAA core–shell nanoparticles favors their potential use in biological applications. Typical TEM images of the PAA-coated UCNPs (**Figure 3**g,h) show that they have a uniform PAA shell with an average thickness of around 2 nm. The minimal increase in particle size, the uniform size distribution, the well-dispersed nature of the nanocomposite, together with the easy synthetic route made the as-obtained UCNP@PAA nanoparticles promising candidates as drug delivery carrier in future biomedical applications.

The presence of the PAA coating was further confirmed by Fourier transform infrared spectroscopy (FTIR) analysis (Figure 3i). In the case of UCNP@PAA, the emergence of a band at 1712 cm^{-1} due to the vibrations of the C = O group indicates that the carboxy groups of PAA have been successfully grafted on the UCNPs. For the DOX-loaded UCNP@PAA, the absorption bands of the stretching vibration of C = O at 1617 and 1578 cm^{-1} from the anthraquinone ring of DOX can be seen, which confirms the successful loading of DOX on UCNP@PAA. Quantitative determination of the polymer content was carried out by thermogravimetry (TG) analysis (Figure 3j). A comparison of the TG data of the UCNPs and UCNP@PAA suggested that 4 wt% of PAA is impregnated on the surface of the UCNPs. The relatively low percentage of 4 wt% in the TG data is in agreement with the thin layer of PAA shell described above.

To highlight the unique pH-controlled drug-delivery properties of UCNP@PAA nanoparticles, the UCNP@$mSiO_2$ nanoparticles were also fabricated according to our previously published method but with minor modifications.[22,23] That is, the UCNPs were directly encapsulated with the mesoporous silica shell through a phase-transfer-assisted surfactant-templating coating process by applying CTAB as the secondary surfactant. Moreover, the thickness of the SiO_2 shell coating can be adjusted from 18 to 12 nm, as shown in the Figure 3a–f, by adjusting the amounts of the reactants, such as TEOS and NaOH. However, further decreasing the thickness of the SiO_2 shell would result in aggregation of the UCNPs, which should of course be avoided. Therefore, the modified UCNP@$mSiO_2$ nanoparticles (with a smallest SiO_2 shell of 12 nm) still have a relatively larger particle size in comparison to the UCNP@PAA nanoparticles (with an average PAA shell of 2 nm). In the following sections, we will make a comparison between UCNP@PAA and UCNP@$mSiO_2$ with regard to the following three

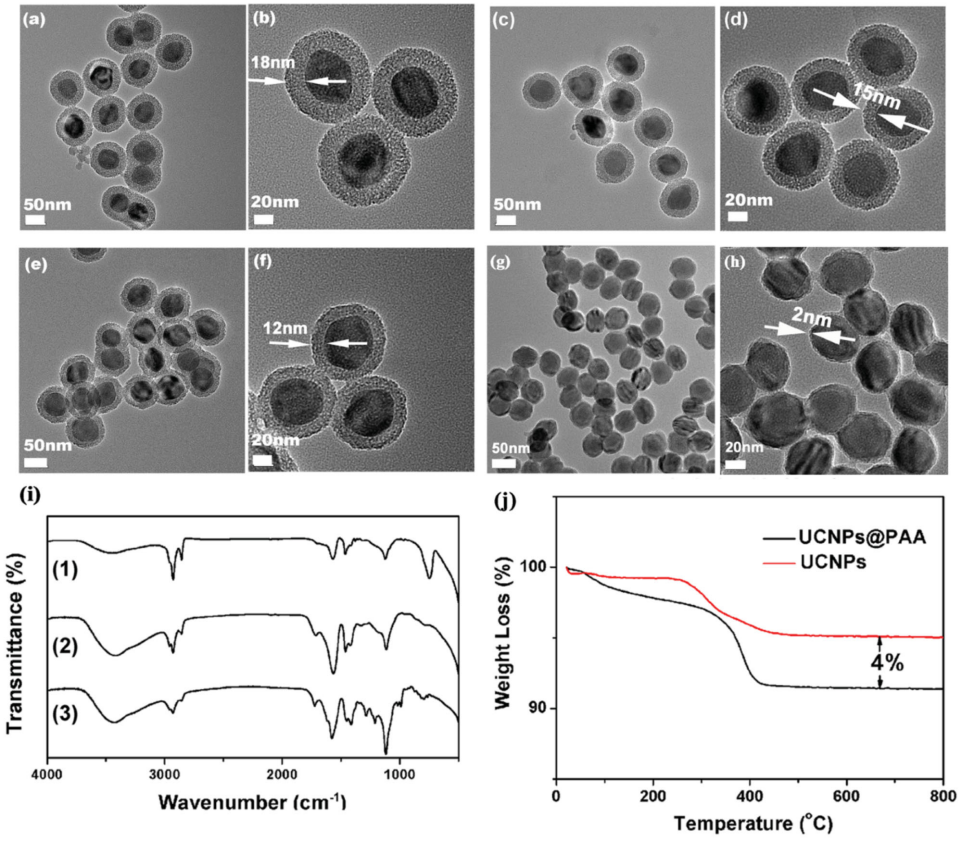

Figure 3. TEM images of UCNP@mSiO_2 nanoparticles with different thicknesses of the SiO_2 shell: a,b) 18 nm; c,d) 15 nm; and e,f) 12 nm. g,h) TEM images of UCNP@PAA with an average PAA shell thickness of around 2 nm. i) FT-IR spectra of UCNPs (1), UCNP@PAA (2), and UCNP@PAA–DOX (3). j) TG analyses of UCNPs and UCNP@PAA.

aspects: drug loading capacity, drug release trends, and in vivo anticancer chemotherapy activity.

2.3. pH-sensitive Drug Release Profiles of UCNP@PAA

The as-obtained UCNP@PAA core–shell nanoparticles can be used as efficient drug delivery carriers owing to their high loading capacity of DOX and sensitive pH-responsive DOX release properties. Before the in vitro drug loading and release experiments, we carried out both pH-dependent zeta-potential and dynamic light scattering (DLS) measurements of UCNP@PAA in order to test their colloidal stability at lower pH. Note that the size distribution results from the DLS measurements are given by intensity. The results show that the zeta potentials of UCNP@PAA nanocomposites increased from –24.5 to +3.2 mV with the pH decreasing from 7.4 to 5.0. Dynamic light scattering measurements of UCNP@PAA for different pH values of the PBS dispersions are also given in Figure S4 of the Supporting Information, indicating that the UCNP@PAA nanoparticles have a good stability at lower pH without much variation in their sizes. It is worth noting that the size observed by DLS was larger than that obtained with the TEM measurements. This is mainly because the size of the nanoparticles obtained by DLS measurements is the hydrodynamic diameter of the nanoparticles swelling in aqueous solution, whereas the diameter obtained by TEM was the diameter of the dried nanoparticles. Next, the in vitro drug loading and controlled release behavior of DOX-loaded UCNP@PAA (labeled as UCNP@PAA–DOX) were carefully studied in phosphate-buffered saline (PBS, pH = 7.4 and 5.0) at 37 °C. The drug loading content was calculated to be 22.8% according to the characteristic DOX optical absorbance at 480 nm, while the in vitro DOX release profiles (**Figure 4**a) were obviously pH-dependent: the cumulative amount of released DOX could reach up to 60% after 48 h at pH 5.0, which is much higher than the 18% at pH 7.4. This means that the UCNP@PAA–DOX nanocomposite exhibited a high encapsulation rate under weakly alkaline conditions with an increased drug dissociation rate under acidic conditions. This tendency was mainly ascribed to the promoted protonation of carboxyl groups in PAA with the decrease of pH, weakening the electrostatic interaction between PAA and DOX.[41] More specifically, in a neutral medium (pH = 7.4) negatively charged PAA would bind with the positively charged DOX by electrostatic interaction. When PAA was protonated to display a positive zeta potential at pH 5.0, this led to the dissociation of the electrostatic interaction between PAA and DOX, subsequently leading to the diffusion of DOX from the UCNP@PAA composite. Since the extracellular pH of solid tumors presents a mild acidic microenvironment in comparison to the

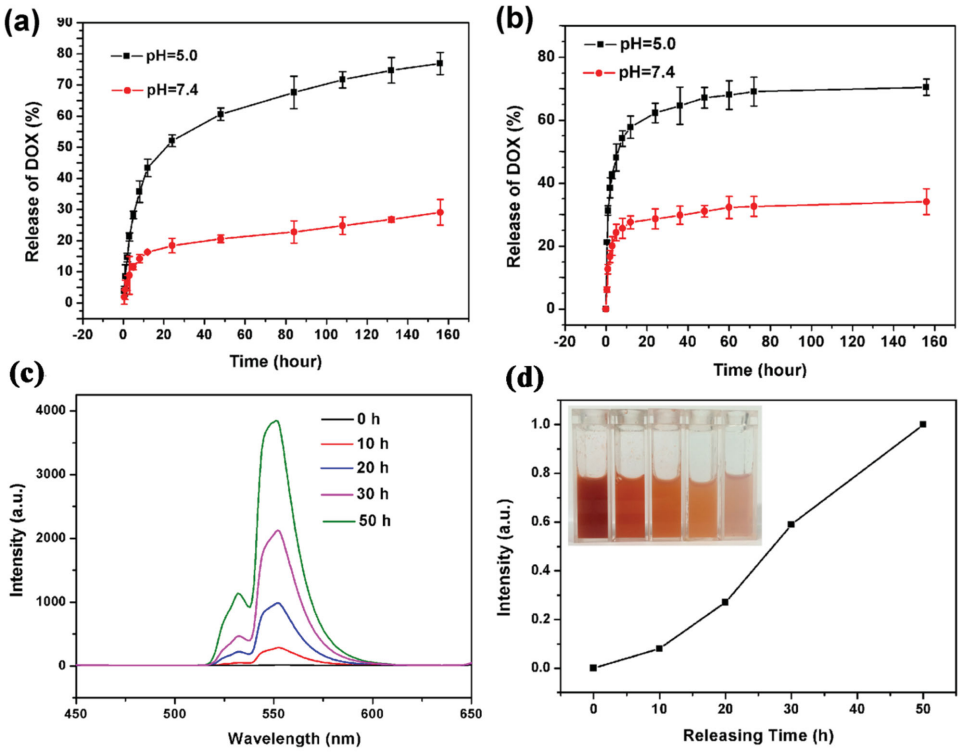

Figure 4. Cumulative DOX release from a) UCNP@PAA and b) UCNP@mSiO$_2$ at pH = 5.0 (black line) and pH = 7.4 (red line) PBS buffer. c) The UC emission spectra of the UCNP@PAA–DOX system at different cumulative release times of DOX. d) The relationship between the UC emission intensity of UCNP@PAA–DOX and the cumulative release time of DOX. The insets in panel (d) are photos of UCNP@PAA–DOX for different cumulative release times of DOX.

physiologically neutral pH of normal tissue, this DOX release tendency is beneficial for the pH-targeted anticancer chemotherapy system.

Since applying a mesoporous silica shell coating on UCNPs is a widely used method to obtain anticancer drug nanocarriers for tumor treatment, the in vitro drug loading and release rate of UCNP@mSiO$_2$–DOX were also investigated in detail (Figure 4b). UCNP@mSiO$_2$ nanoparticles with an average SiO$_2$ thickness of 12 nm were chosen for the following experiments. The results show that: i) the drug loading content of UCNP@mSiO$_2$–DOX was calculated to be 7.9%, much lower than that of UCNP@PAA–DOX; ii) the drug release rate of UCNP@mSiO$_2$–DOX was also clearly pH-dependent because of the increased hydrophilicity of DOX at lower pH. This pH-dependent DOX release trend is similar to that of UCNP@PAA–DOX, but with a relatively high DOX release speed, which is not beneficial for maintaining the concentration of the drug within the therapeutic window. Concluding, the relatively low drug loading and rapid release speed of DOX limit bio-applications of UCNP@mSiO$_2$, whereas UCNP@PAA nanoparticles constitute a much more promising platform for designing a pH-dependent drug delivery system for anticancer therapy.

Moreover, one of the major advantages of utilizing UCNP-based composites as drug carriers is that UCNPs allow tracking and evaluating of the efficiency of the drug release in real time.[41] Therefore, we also investigated the relationship between the UC emission intensity of the UCNP@PAA–DOX system and the cumulative release time of DOX. As shown in Figure 4c and 4d, the UC emission intensity increases with increasing cumulative amount of released DOX. This is because the DOX molecules loaded in UCNP@PAA have high phonon energies, thus quenching some luminescent centers of the UCNPs. With the cumulative released dosages of DOX from the DOX–UCNP@PAA system, the number of quenched luminescent centers would decrease, leading to a regaining of the emission intensity. This correlation between the UC luminescence intensity and the extent of the drug release can potentially be used as a probe for monitoring drug release movements during disease therapy.

2.4. In Vitro Cytotoxic Effect against Cancer Cells and UCL Imaging of UCNP@PAA

Since the cytotoxicity of drug delivery carriers is an important prerequisite and crucial factor for future bioapplications,[42,43] the in vitro cytotoxicity of the UCNP@PAA was carried out by a standard MTT assay on MCF-7 cells. As shown in Figure S5 of the Supporting Information, even after the 24 h or 48 h culture, MCF-7 cells were not impaired significantly at concentrations as high as 200 μg mL^{-1}. This observation suggests that UCNP@PAA nanoparticles have good biocompatibility to satisfy the requirements as potential drug carriers for biological applications. To further investigate the in vitro cytotoxic effects of UCNP@PAA–DOX, culture mediums containing pure DOX, UCNP@PAA–DOX, and pure UCNP@PAA nanoparticle

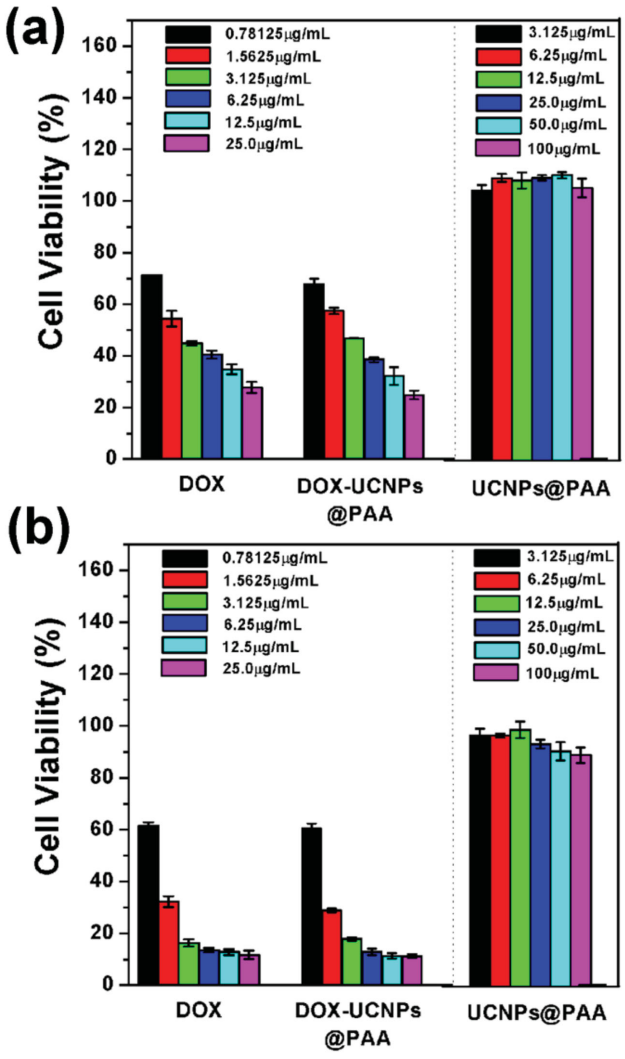

Figure 5. In vitro cytotoxicity of free DOX, UCNP@PAA–DOX, and pure UCNP@PAA against MCF-7 cells after a) 24 h and b) 48 h incubation.

solutions were added into each well of a 96-well plate, followed by further incubation for another 24 and 48 h. **Figure 5** shows that the DOX-loaded UCNP@PAA after cultures of 24 or 48 h had a comparable or even higher cytotoxicity than free DOX at the same concentration of DOX, which indicated that the UCNP@PAA–DOX was pharmacologically active as a potential drug nanocarrier.

Moreover, the UCL imaging properties of the as-obtained UCNP@PAA nanoparticles were studied as well. The UCL spectra of the original UCNPs in chloroform, CTAB-exchanged UCNPs, and PAA-coated UCNPs in water are given in Figure S6 of the Supporting Information. All experimental conditions were kept identical in order to avoid experimental errors. From Figure S6 we can see that the upconversion intensity of the aqueous solution of UCNP-CTAB decreased to about 40% of the original intensity in chloroform solution before CTAB modification. This is mainly due to an increase in the multiphonon relaxation in aqueous media caused by high-energy vibration of water molecules. After the successful coating of PAA, the upconversion intensity of as-obtained UCNP@PAA further decreased, which can be ascribed to the quenching effect of the PAA coating. In spite of this, the UCL intensity of UCNP@PAA is still high enough to satisfy the requirements for in vitro/in vivo bioimaging. In order to verify the in vitro UCL imaging properties of UCNP@PAA nanomaterials,[44] inverted fluorescence microscopy was carried out (**Figure 6**) on MCF-7 cells incubated with UCNP@PAA (100 μg mL^{-1}) for 10 min, 3 h, and 6 h. An obviously increasing UCL signal can be observed over the course of time under NIR laser excitation, indicating that more nanoparticles were incubated into the MCF-7 cells. This finding indicates that UCNP@PAA can be used as an excellent luminescence probe for cell imaging and monitoring the cell endocytosis process. Furthermore, green light emission can also be clearly seen in vivo under 808-nm laser irradiation, even in daylight after intratumoral injection of UCNP@PAA nanoparticles, as shown in Figure S7 of the Supporting Information, which indicates that the as-obtained nanocomposites show effective tissue penetration and excellent upconversion luminescence properties.[45]

2.5. In Vivo Antitumor Efficacy of DOX Loaded UCNP@PAA

After having demonstrated the chemotherapy effects in vitro, we investigated whether UCNP@PAA–DOX could be an effective antitumor formulation in vivo. A H22 (murine hepatocarcinoma) xenograft model developed by injecting H22 cancer cells in the left axilla of Kunming mice was carried out to investigate the antitumor efficacy of DOX-loaded UCNP@PAA. Twenty mice bearing tumors were randomly divided into four groups and treated with saline solution (as control), pure DOX, UCNP@$mSiO_2$–DOX and UCNP@PAA–DOX, respectively. Note that the group that was administered UCNP@$mSiO_2$–DOX was added to this experiment to make a comparison with the in vivo antitumor effects of UCNP@PAA–DOX. During the experiments, no mice died. The trend variations of the mean body weights and relative tumor volumes in each group are shown in **Figure 7**a,b. The weight of the mice (Figure 7a) increased steadily with time and the increasing trends of those four groups were similar. However, the mean relative tumor volumes of each group varied (Figure 7b): a fast tumor growth curve was obtained in the control group while for the other three groups the tumor growth rates decreased to a certain degree. Among them, the tumor growth in the mice treated with UCNP@PAA–DOX was dramatically inhibited with almost no apparent growth over the 14-day interval, much lower than that of the pure DOX and UCNP@$mSiO_2$–DOX groups. These results again demonstrated the efficacy of the UCNP@PAA for use as a nanocarrier platform in chemotherapy.

The above conclusions were further verified by photographs and average weights of the final tumors excised from mice of each group. As shown in Figure 7c,d, the group treated with UCNP@PAA–DOX had an average tumor growth inhibition efficacy of approximately 89%, much higher than both the UCNP@$mSiO_2$–DOX group with an inhibition efficacy of 75% and the pure DOX group with about 70%. The results were attributed to the unique properties of the UCNP@PAA drug carriers, such as the relatively small nanoparticle size,

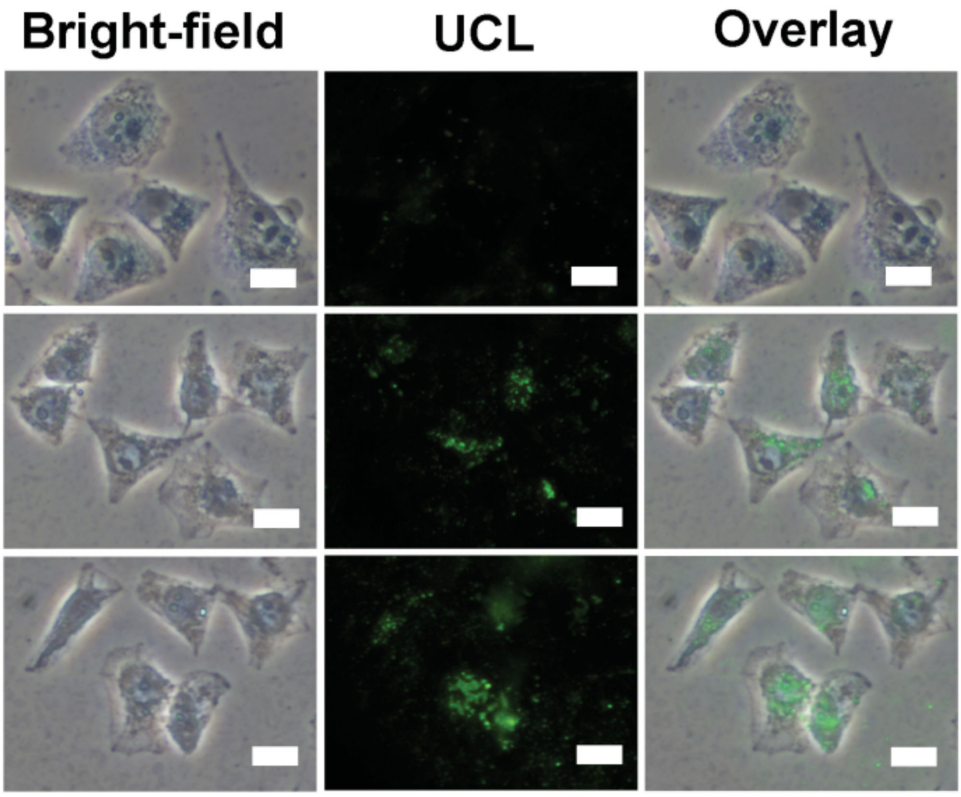

Figure 6. Inverted florescence microscopy images of MCF-7 cells incubated with UCNP@PAA for 10 min, 3 h, and 6 h at 37 °C under 808-nm irradiation. Each series shows a bright-field image, upconversion luminescent image (UCL), and the overlay, and corresponds from top to bottom with the times mentioned above, respectively. All scale bars are 20 μm.

enhanced permeability and retention effect (EPR), high drug loading capacity, sustained and pH-sensitive drug release curve, and so on. Haematoxylin and eosin (H&E) staining of tumor slices was also carried out for tumors collected after the various treatments (Figure 7e). As expected, significant cancer cell damage was noticed in the group of UCNP@PAA–DOX, while cells in both control groups and the UCNP@PAA group largely retained their normal morphology with distinctive membrane and nuclear structures.[46,47] Those results are in good agreement with the tumor growth data, further confirming the superior anti-cancer chemotherapeutic efficacy of UCNP@PAA–DOX. The histological analysis data shown in **Figure 8** reveal that no pathological changes occurred in the main organs of heart, liver, spleen, lung, and kidney. Both hepatocytes in the liver samples and the glomerulus structure in the kidney section were found to be normal, while pulmonary fibrosis was not detected in the lung samples. Necrosis was not observed in any of the histological samples analyzed. The above results indicate that the UCNP@PAA nanoparticles have excellent in vivo biocompatibility and could be used as a highly active drug-delivery carrier for anticancer therapy.[48]

3. Conclusions

We have successfully fabricated uniform UCNP@PAA nanoparticles that feature a highly effective 808-nm excited UCNP core and a thin shell of PAA that can be used simultaneously for upconversion bioimaging and anticancer chemotherapy. It was found that the optimal core–shell 808-nm-to-visible UCNP nanocomposition shows a relatively high absolute upconversion quantum yield of 0.18% under green-emission conditions; this optimal nanocomposite architecture was obtained by elaborate optimization of parameters such as core size, the number of encapsulation layers, and the choice of host lattices. A significant 12.8× improvement of the UCL intensity was obtained in our novel nanocomposite system comparing with Er@Y@Nd nanoparticles. When coated with a thin layer of PAA, the resulting uniform UCNP@PAA nanocomposites show better performances as pH-responsive anticancer drug delivery carriers in comparison with UCNP@mSiO_2 nanoparticles, which has been evidenced by in vitro/in vivo tests. Summarizing, the as-obtained UCNP@PAA nanocomposites represent a major step forward towards anti-tumor chemotherapy that utilizes 808-nm excited UCNPs to access the tumors effectively without causing detrimental overheating effects.

4. Experimental Section

Materials: All chemical reagents were directly used without further purification. The rare earth oxides Y_2O_3, Yb_2O_3, Gd_2O_3, and Er_2O_3 were purchased from Science and Technology Parent Company of Changchun

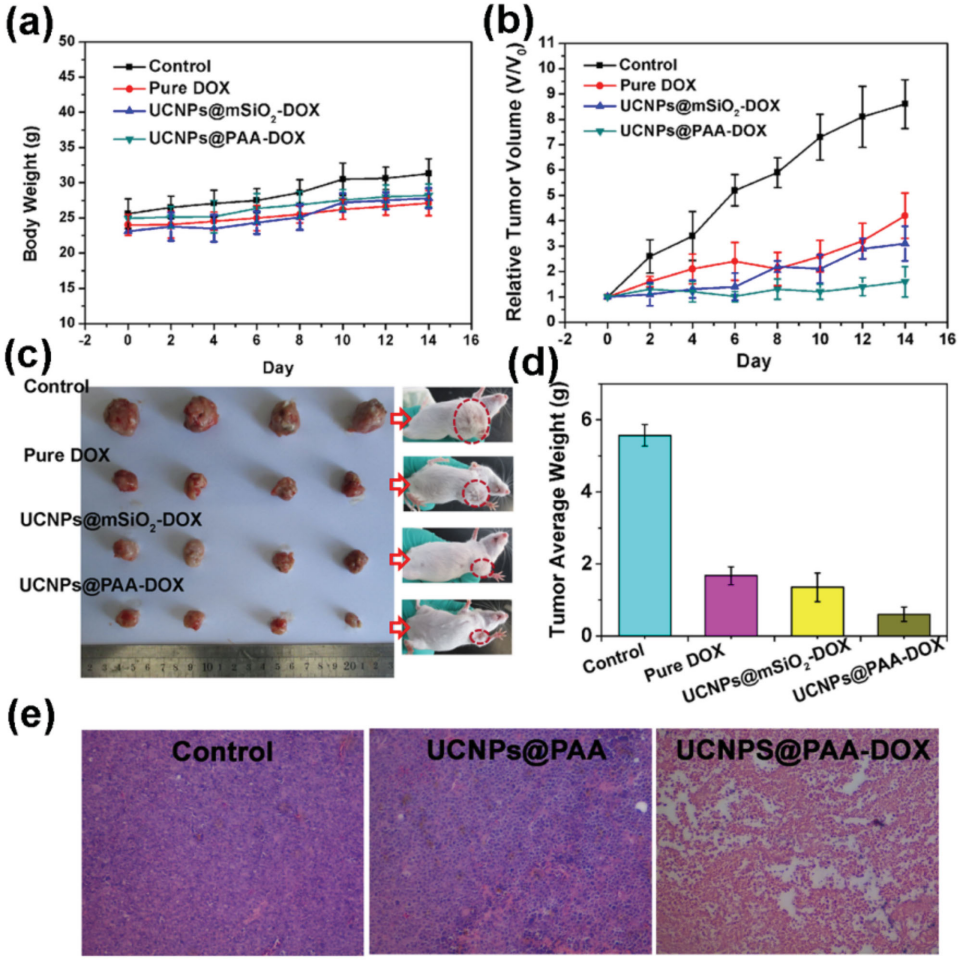

Figure 7. a) Body weight and b) relative tumor volume of mice after treatment with a saline solution as control, pure DOX, UCNP@$mSiO_2$–DOX, and UCNP@PAA–DOX, respectively. c) Photographs of excised tumors from representative euthanized mice and d) mean tumor weights of each group from the last day of the experiment. e) Haematoxylin and eosin (H&E) staining of tumor slices for the control, UCNP@PAA, and UCNP@PAA–DOX groups, respectively.

Institute of Applied Chemistry. Sodium oleate ($C_{15}H_{33}NaO_2$), sodium fluoride (NaF), Oleic acid (OA), cetyltrimethylammonium bromide (CTAB), tetraethylorthosilicate (TEOS), ammonium nitrate (NH_4NO_3), sodium hydroxide (NaOH), ammonium fluoride (NH_4F), ammonium hydroxide ($NH_3{\cdot}H_2O$), anhydrous ethanol, isopropyl alcohol, n-hexane, and cyclohexane were all purchased from the Beijing Chemical Reagent Company. Trifluoroacetic acid (CF_3COOH), oleic acid (OA), and octadecene (ODE) were purchased from Aldrich. Doxorubicin hydrochloride (DOX) was purchased from Nanjing Duodian Chemical Limited Company (China). Polyacrylic acid (PAA, Mw ≈ 1800) was obtained from Sigma-Aldrich. The rare-earth trifluoroacetates were prepared by dissolving the corresponding rare-earth oxides in trifluoroacetic acid (CF_3COOH) at elevated temperature, followed by evaporating the solvent at 80 °C for 10 h. The as-obtained rare-earth trifluoroacetates were stored for further use. The rare-earth oleate complexes were synthesized according to a method from the literature[49] with a little modification.

Synthesis of the Core–Shell UCNPs: The core nanoparticles $NaYF_4$:18%Yb,2%Er were synthesized by thermal decomposition methodology developed by Chen et al.[50] The as-obtained nanoparticles were precipitated by addition of an excess amount of ethanol, then collected by centrifugation, and subsequently redispersed in 2 mL of cyclohexane. We used a general procedure for the epitaxial growth of shell layers; here we took $NaYF_4$:Yb, Er@$NaYF_4$:Yb as example. The growth of the other shell layers was carried out with similar procedures. The $NaYF_4$:Yb shell growth process was as follows: 2 mL of cyclohexane solution containing the as-obtained core nanocrystals was added into a mixture solution of 10 mL of OA and 10 mL of ODE in a 100-mL four-neck round-bottom reaction vessel, followed by heating at 120 °C under vacuum under magnetic stirring for 30 min in order to remove residual water and oxygen totally. Next, the solution was heated to 310 °C under a N_2 atmosphere. During the process of heating up, the shell precursors including 0.5 mmol of $RE(CF_3COO)_3$ (RE = 90% Y+10% Yb) and 0.5 mmol of CF_3COONa were dissolved in 4 mL OA/ODE (v:v = 1:1), then injected into the above reaction solution dropwise when the temperature reached 310 °C. The reaction was kept at this temperature for 1 h. The above procedures were repeated for the layer-by-layer growth of the multi-shell nanoparticles. Finally, the as-obtained transparent yellowish reaction mixture was cooled down to 60 °C, precipitated by addition of enough ethanol, collected by centrifugation, and re-dispersed in 20 mL of chloroform.

Measurement of the Upconversion Quantum Yield (QY): For the measurement of the upconversion quantum yield, the samples were excited with a 808-nm diode laser at a power density of 31 W cm^{-2}. The UCL emission peaks in the spectral range of 400–720 nm for Er^{3+} were integrated for calculating the QY. All spectral data collected were corrected for the spectral response of both the spectrometer (QE65000, Ocean Optics) and the integrating sphere by a standard tungsten lamp. The quantum yield (QY) is defined as:

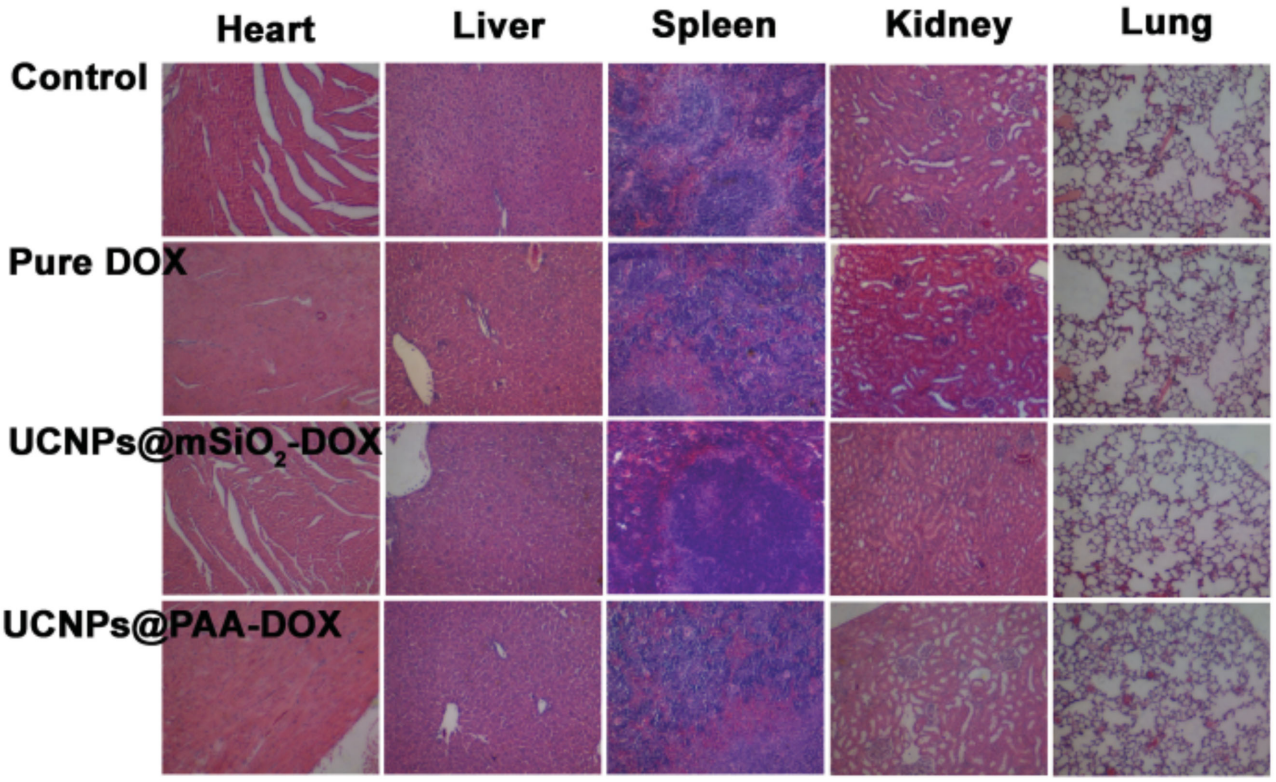

Figure 8. Hematoxylin and eosin (H&E) stained images of major organs for control, pure DOX, UCNP@mSiO$_2$–DOX, and UCNP@PAA–DOX groups.

$$\begin{aligned} QY &= (\text{photons emitted}) / (\text{photons absorbed}) \\ &= (L_{sample}) / (E_{reference} - E_{sample}) \end{aligned} \quad (1)$$

where L_{sample} is the emission intensity, $E_{reference}$ and E_{sample} are the intensities of the incident light not absorbed by the sample and the reference sample, respectively.

Synthesis of UCNP@PAA and UCNP@mSiO$_2$ Nanoparticles: The as-prepared oleic-acid stabilized UCNPs nanocrystals should first undergo a phase transfer from chloroform to water by adding 2 mL of the UCNP chloroform solution to an aqueous solution containing 0.1 g CTAB and 20 mL water. The mixture was then stirred vigorously for 2 h to evaporate cyclohexane solvent, resulting in the formation of a UCNP–CTAB water solution. UCNP@PAA was successfully synthesized according to a literature method[51] with minor modifications. In detail, the as-prepared CTAB-capped UCNPs were collected by centrifugation, washed with water several times, and re-dispersed in 10 mL of deionized water. The 30 µL of PAA aqueous solution (0.2 g mL^{-1}) and 45 µL of $NH_3{\cdot}H_2O$ (2 mol L^{-1}) were then added to the UCNP–CTAB aqueous solution, followed by ultrasonic dispersion for 30 min. Finally, 40 mL of isopropyl alcohol was dripped into the above mixed solution under magnetic stirring in order to obtain the UCNP@PAA nanoparticles. UCNP@SiO$_2$ nanoparticles were synthesized as follows: 3 mL of ethanol, 150 µL of NaOH solution (2 M), and 200 µL of TEOS were added in sequence into 30mL of UCNP–CTAB water solutions and maintained at 70 °C for 1 h under vigorous magnetic stirring. In order to remove the pore-generating template CTAB, the as-obtained UCNP@SiO$_2$ nanoparticles re-dispersed in NH_4NO_3 ethanol solution at 60 °C for 4 h. The final synthesized UCNP@mSiO$_2$ nanoparticles were dispersed in 20 mL of ethanol.

In Vitro Drug Storage and Release: In vitro drug storage of UCNP@PAA and UCNP@mSiO$_2$ nanoparticles was carried out by mixing the UCNP@PAA or UCNP@mSiO$_2$ with 2 mL of DOX solution (1 mg mL^{-1}) under magnetic stirring overnight at 37 °C. The obtained DOX-loaded nanoparticles were collected by centrifugation at 6000 rpm for 5 min and denoted as UCNP@PAA–DOX and UCNP@mSiO$_2$–DOX. The in vitro drug release experiments were carried out as follows: the as-obtained DOX loaded nanoparticles were collected by centrifugation and re-dispersed in 2 mL of pH = 7.4 and 5.0 phosphoric buffer solutions (PBS) under magnetic stirring, respectively. At predetermined time intervals, such as 30 min, 1 h, 2 h, 3 h, etc., 2 mL of fresh PBS was replaced for the original PBS and the as-obtained original PBS was measured by UV–Vis spectral measurement in order to determine the amount of the released DOX.

In Vitro Cytotoxicity of UCNP@PAA and UCNP@PAA–DOX: A typical MTT [3-(4,5-dimethylthiazol-2-yl)-2,5-diphenyltetrazolium bromide] cell assay was carried out to investigate the in vitro cytotoxicity of UCNP@PAA and UCNP@PAA–DOX. Briefly, MCF-7 cells were seeded in a 96-well plate (6000 cells per well) and incubated in a humidified atmosphere of 5% CO_2 overnight to ensure that the cells had attached to the wells. After that, different materials, such as free DOX, UCNP@PAA–DOX and pure UCNP@PAA, with different concentrations, were added to each well of the 96-well plate, followed by further incubation for another 24 and 48 h. The concentrations of DOX were 0.78125, 1.5625, 3.125, 6.25, 12.5, and 25 µg mL^{-1}, while the corresponding concentrations of pure UCNP@PAA were 3.125, 6.25, 12.5, 25, 50, and 100 µg mL^{-1}, respectively. The following steps were then followed by the typical steps of the MTT cell assay: MTT solution (20 µL, 5 mg mL^{-1}) was added to each well, further incubated for 4 h, and then 150 µL of DMSO were added after removing the original culture medium. The final fraction surviving of MCF-7 cells was measured by a microplate reader at the wavelength of 490 nm.

In Vitro UCL Imaging of UCNP@PAA: The in vitro upconversion luminescence imaging of MCF-7 cells was carried out by a custom-built instrument for upconversion luminescence microscopy, which was rebuilt from an inverted fluorescence microscope (Nikon Ti-S) with an external laser diode for illuminating the samples. MCF-7 cells were seeded in 6-well culture plates (6×10^4 cells per well) and incubated (37 °C, 5% CO_2) overnight. Then the original cell culture medium was

discarded and fresh culture medium containing UCNP@PAA solution (2 mL, 100 μg mL^{-1}) was added into each well and incubated at 37 °C for 10 min, 3 h, and 6 h, respectively. Then, the cells were carefully washed with PBS three times, fixed with 4% poly formaldehyde PBS solution for 15 min, and then washed with PBS three times again.

In Vivo Antitumor Efficacy of UCNP@PAA–DOX and UCNP@mSiO$_2$–DOX: Female Kunming mice (about 20 g) were purchased from the Center of Experimental Animals, Jilin University (Changchun, China), and the animal experiments agreed well with the criterions of The National Regulation of China for Care and Use of Laboratory Animals. The tumors were established by subcutaneous injection of H22 cells (murine hepatocarcinoma cell lines) in the left axilla of the mice. The tumor-bearing mice were randomly divided into four groups ($n = 5$, each group) after the tumors grew to a size of around 100–200 mm^3, and treated with saline as control, pure DOX, UCNP@mSiO$_2$–DOX and UCNP@PAA–DOX by tail vein injection respectively. We injected the above materials three times on day 0, 3, and 5, respectively, and at each time point the injected DOX dose was 4.0 mg kg^{-1} body weight. The body weights and tumor volumes of each mouse were monitored every two days and 14 days later, the tumors were dissected and weighed to evaluate the therapeutic efficacy. In a typical calculation, the tumor volume was calculated by: tumor volume (V) = (length × width^2)/2. The relative tumor volume was calculated as V/V_0, where the V_0 was the corresponding tumor volume before the treatment. Tumor growth inhibition rate was determined as $(C - T)/C \times 100\%$, in which C was the average tumor weight of the control group while T is the average tumor weight of each treated group. Finally, the mean organs of mice, such as liver, spleen, heart, lung, and kidney, were removed and fixed in 4% paraformaldehyde solution for histological examination in order to further investigate the biocompatibility of UCNP@PAA and UCNP@mSiO$_2$.

Characterization: The X-ray diffraction (XRD) patterns of the samples were carried out on a D8 Focus diffractometer (Bruker) with use of Cu Kα radiation (λ = 0.15405 nm). The UV–vis adsorption spectra values were measured on a U-3310 spectrophotometer. Transmission electron microscopy (TEM) images were obtained on a FEI Tecnai G2 S-Twin transmission electron microscope with a field emission gun operating at 200 kV. Nitrogen adsorption/desorption analysis was measured using a Micromeritics ASAP 2020 M apparatus. FT-IR spectra were performed on a Perkin-Elmer 580B infrared spectrophotometer using the KBr pellet technique. Thermogravimetry (TG) was carried out on a Netzsch Thermoanalyzer STA 409 instrument in an atmospheric environment with a heating rate of 10 °C min^{-1} from room temperature to 800 °C. All dynamic light scattering (DLS) and zeta potential distribution measurements were carried out on a Zetasizer Nano ZS (Malvern Instruments Ltd., UK). The UCL emission spectra were obtained by an F-7000 spectrophotometer (Hitachi) equipped with a 808-nm laser diode as the excitation source, and the data were recorded from 300 to 750 nm. MTT experiments were carried out by a microplate reader (Therom Multiskan MK3). The instrument of UCLM was rebuilt on an inverted fluorescence microscope (Nikon Ti-S), and an external 808-nm diode laser was used to illuminate the samples. All measurements were performed at room temperature.

Supporting Information

Supporting Information is available from the Wiley Online Library or from the author.

Acknowledgements

This project is financially supported by the National Natural Science Foundation of China (NSFC 51332008, 51372243, 51422209, 51202239) and the National Basic Research Program of China (2014CB643803).

Received: April 20, 2015
Revised: May 24, 2015
Published online: June 25, 2015

[1] Y. S. Liu, D. T. Tu, H. M. Zhu, X. Y. Chen, *Chem. Soc. Rev.* **2013**, *42*, 6924.
[2] W. Zheng, P. Huang, D. T. Tu, E. Ma, H. M. Zhu, X. Y. Chen, *Chem. Soc. Rev.* **2015**, *44*, 1379.
[3] D. J. Gargas, E. M. Chan, A. D. Ostrowski, S. Aloni, M. V. P. Altoe, E. S. Barnard, B. Sanii, J. J. Urban, D. J. Milliron, B. E. Cohen, P. J. Schuck, *Nat. Nanotechnol.* **2014**, *9*, 300.
[4] Z. J. Gu, L. Yan, G. Tian, S. J. Li, Z. F. Chai, Y. L. Zhao, *Adv. Mater.* **2013**, *25*, 3758.
[5] Y. Sun, X. J. Zhu, J. J. Peng, F. Y. Li, *ACS Nano* **2013**, *7*, 11290.
[6] F. Zhang, R. C. Che, X. M. Li, C. Yao, J. P. Yang, D. K. Shen, P. Hu, W. Li, D. Y. Zhao, *Nano Lett.* **2012**, *12*, 2852.
[7] R. Wang, X. M. Li, L. Zhou, F. Zhang, *Angew. Chem. Int. Ed.* **2014**, *53*, 12086.
[8] F. Chen, W. B. Bu, S. J. Zhang, X. H. Liu, J. N. Liu, H. Y. Xing, Q. F. Xiao, L. J. Zhou, W. Peng, L. Z. Wang, J. L. Shi, *Adv. Funct. Mater.* **2011**, *21*, 4285.
[9] J. P. Lai, Y. X. Zhang, N. Pasquale, K. B. Lee, *Angew. Chem. Int. Ed.* **2014**, *53*, 14419.
[10] X. J. Xie, N. Y. Gao, R. R. Deng, Q. Sun, Q. H. Xu, X. G. Liu, *J. Am. Chem. Soc.* **2013**, *135*, 12608.
[11] J. Shen, G. Y. Chen, A. M. Vu, W. Fan, O. S. Bilsel, C. C. Chang, G. Han, *Adv. Opt. Mater.* **2013**, *1*, 644.
[12] L. D. Sun, Y. F. Wang, C. H. Yan, *Acc. Chem. Res.* **2014**, *47*, 1001.
[13] M. K. G. Jayakumar, N. M. Idris, K. Huang, Y. Zhang, *Nanoscale* **2014**, *6*, 8441.
[14] M. Pokhrel, L. C. Mimun, B. Yust, G. A. Kumar, A. Dhanale, L. Tang, D. K. Sardar, *Nanoscale* **2014**, *6*, 1667.
[15] H. L. Wen, H. Zhu, X. Chen, T. F. Hung, B. L. Wang, G. Y. Zhu, S. F. Yu, F. Wang, *Angew. Chem. Int. Ed.* **2013**, *52*, 13419.
[16] R. Arppe, T. Nareoja, S. Nylund, L. Mattsson, S. Koho, J. M. Rosenholm, T. Soukka, M. Schaferling, *Nanoscale* **2014**, *6*, 6837.
[17] T. V. Esipova, X. Ye, J. E. Collins, S. Sakadžić, E. T. Mandeville, C. B. Murray, S. A. Vinogradov, *Proc. Natl. Acad. Sci. U.S.A.* **2012**, *109*, 20826.
[18] X. M. Liu, X. G. Kong, Y. L. Zhang, L. P. Tu, Y. Wang, Q. H. Zeng, C. G. Li, Z. Shi, H. Zhang, *Chem. Commun.* **2011**, *47*, 11957.
[19] S. Wang, L. Zhang, C. H. Dong, L. Su, H. J. Wang, J. Chang, *Chem. Commun.* **2015**, *51*, 406.
[20] J. F. Jin, Y. J. Gu, C. W. Y. Man, J. P. Cheng, Z. H. Xu, Y. Zhang, H. S. Wang, V. H. Y. Lee, S. H. Cheng, W. T. Wong, *ACS Nano* **2011**, *5*, 7838.
[21] W. P. Fan, B. Shen, W. B. Bu, F. Chen, K. L. Zhao, S. J. Zhang, L. P. Zhou, W. J. Peng, Q. F. Xiao, H. Y. Xing, J. N. Liu, D. L. Ni, Q. J. He, J. L. Shi, *J. Am. Chem. Soc.* **2013**, *135*, 6494.
[22] B. Liu, C. X. Li, P. A. Ma, Y. Y. Chen, Y. X. Zhang, Z. Y. Hou, S. S. Huang, J. Lin, *Nanoscale* **2015**, *7*, 1839.
[23] C. X. Li, D. M. Yang, P. A. Ma, Y. Y. Chen, Y. Wu, Z. Y. Hou, Y. L. Dai, J. H. Zhao, C. P. Sui, J. Lin, *Small* **2013**, *9*, 4150.
[24] Y. H. Wang, S. Y. Song, J. H. Liu, D. P. Liu, H. J. Zhang, *Angew. Chem. Int. Ed.* **2014**, DOI: 10.1002/anie.201409519.
[25] H. Y. Chen, B. Qi, T. Moore, F. L. Wang, D. C. Colvin, L. D. Sanjeewa, J. C. Gore, S. J. Hwu, O. T. Mefford, F. Alexis, J. N. Anker, *Small* **2014**, *10*, 3364.
[26] L. Yuan, Q. Q. Tang, D. Yang, J. Z. Zhang, F. Y. Zhang, J. H. Hu, *J. Phys. Chem. C* **2011**, *115*, 9926.
[27] C. H. Liu, Z. Wang, X. K. Wang, Z. P. Li, *Sci. China Chem.* **2011**, *54*, 1292.
[28] X. Chen, A. H. Soeriyadi, X. Lu, S. M. Sagnella, M. Kavallaris, J. J. Gooding, *Adv. Funct. Mater.* **2014**, *24*, 6999.
[29] X. J. Kang, D. M. Yang, Y. L. Dai, M. M. Shang, Z. Y. Cheng, X. Zhang, H. Z. Lian, P. A. Ma, J. Lin, *Nanoscale* **2013**, *5*, 253.

[30] L. Li, C. Liu, L. Y. Zhang, T. T. Wang, H. Yu, C. G. Wang, Z. M. Su, *Nanoscale* **2013**, *5*, 2249.
[31] L. L. Chen, L. Li, L. Y. Zhang, S. X. Xing, T. T. Wang, Y. A. Wang, C. G. Wang, Z. M. Su, *ACS Appl. Mater. Interfaces* **2013**, *5*, 7282.
[32] Y. T. Zhong, G. Tian, Z. J. Gu, Y. J. Yang, L. Gu, Y. L. Zhao, Y. Ma, J. N. Yao, *Adv. Mater.* **2014**, *26*, 2831.
[33] Y. F. Wang, G. Y. Liu, L. D. Sun, J. W. Xiao, J. C. Zhou, C. H. Yan, *ACS Nano* **2013**, *7*, 7200.
[34] X. J. Xie, N. Y. Gao, R. R. Deng, Q. Sun, Q. H. Xu, X. G. Liu, *J. Am. Chem. Soc.* **2013**, *135*, 12608.
[35] X. M. Li, R. Wang, F. Zhang, L. Zhou, D. K. Shen, C. Yao, D. Y. Zhao, *Sci. Rep.* **2013**, *3*, 3536.
[36] Y. X. Liu, D. S. Wang, L. L. Li, Q. Peng, Y. D. Li, *Inorg. Chem.* **2014**, *53*, 3257.
[37] N. J. J. Johnson, F. C. J. M. van Veggel, *ACS Nano* **2014**, *8*, 10517.
[38] H. Y. Chen, B. Qi, T. Moore, D. C. Colvin, T. Crawford, J. C. Gore, F. Alexis, O. T. Mefford, J. N. Anker, *Small* **2014**, *10*, 160.
[39] C. H. Dong, A. Korinek, B. Blasiak, B. Tomanek, F. C. J. M. van Veggel, *Chem. Mater.* **2012**, *24*, 1297.
[40] X. K. Jia, J. J. Yin, D. G. He, X. X. He, K. M. Wang, M. Chen, Y. H. Li, *J. Biomed. Nanotechnol.* **2013**, *9*, 1.
[41] D. M. Yang, P. A. Ma, Z. Y. Hou, Z. Y. Cheng, C. X. Li, J. Lin, *Chem. Soc. Rev.* **2015**, *44*, 1416.
[42] S. Venkatraman, *Nanotechnology* **2014**, *25*, 372501.
[43] C. X. Li, Z. Y. Hou, Y. L. Dai, D. M. Yang, Z. Y. Cheng, P. A. Ma, J. Lin, *Biomater. Sci.* **2013**, *1*, 213.
[44] B. Liu, C. Li, D. Yang, Z. Hou, P. a. Ma, Z. Cheng, H. Lian, S. Huang, J. Lin, *Eur. J. Inorg. Chem.* **2014**, *2014*, 1906.
[45] G. Y. Chen, H. L. Qiu, P. N. Prasad, X. Y. Chen, *Chem. Rev.* **2014**, *114*, 5161.
[46] L. Xia, X. G. Kong, X. M. Liu, L. P. Tu, Y. L. Zhang, Y. L. Chang, K. Liu, D. Z. Shen, H. Y. Zhao, H. Zhang, *Biomaterials* **2014**, *35*, 4146.
[47] C. Wang, H. Xu, C. Liang, Y. M. Liu, Z. W. Li, G. B. Yang, L. Cheng, Y. G. Li, Z. Liu, *ACS Nano* **2014**, *7*, 6782.
[48] L. Q. Xiong, T. S. Yang, Y. Yang, C. J. Xu, F. Y. Li, *Biomaterials* **2010**, *31*, 7078.
[49] J. Park, K. An, Y. Hwang, J. G. Park, H. J. Noh, J. Y. Kim, J. H. Park, N. M. Hwang, T. Hyeon, *Nat. Mater.* **2004**, *3*, 891.
[50] Y. Wei, F. Q. Lu, X. R. Zhang, D. P. Chen, *Chem. Mater.* **2006**, *18*, 5733.
[51] L. Li, L. Y. Zhang, S. X. Xing, T. T. Wang, S. R. Luo, X. Q. Zhang, C. Liu, Z. M. Su, C. G. Wang, *Small* **2013**, *9*, 825.